



Nano-scale structural studies of defects in arsenic-implanted n and p-type HgCdTe films

I. Izhnin¹ · A. V. Voitsekhovskii² · A. G. Korotaev² · K. D. Mynbaev³ · Z. Swiatek⁴ · J. Morgiel⁴ · O. I. Fitsych⁵ · V. S. Varavin⁶ · D. V. Marin⁶ · M. V. Yakushev⁶ · O. Yu. Bonchuk⁷ · H. V. Savvitsky⁷

Received: 23 October 2020 / Accepted: 27 January 2021 / Published online: 9 February 2021
© King Abdulaziz City for Science and Technology 2021

Abstract

Bright-field and high-resolution transmission electron microscopy were used for nano-scale structural studies of defects induced by implantation of arsenic ions with 190 keV energy and 10^{14} cm⁻² fluence in n and p-type Hg_{0.78}Cd_{0.22}Te films grown by molecular-beam epitaxy. A similarity in defect pattern formed by arsenic implantation in n and p-type material was observed. The electrical properties of the implanted layers in n and p-type films also appeared to be similar, confirming the results of microscopic observations.

Keywords HgCdTe · Arsenic implantation · Transmission electron microscopy · Defects

Introduction

Ion implantation is the method of choice for ex situ fabrication of p–n junctions in Hg_{1-x}Cd_xTe (MCT), one of the most important materials for infrared photo-electronics. Recently, there has been much interest in photodiodes based on arsenic implantation in MCT with n–type conductivity (Gravrand et al. 2009; Mollard et al. 2011; Park et al. 2016; Bazovkin et al. 2016; Bommena et al. 2015; Guinedor et al. 2019). Dark currents in ‘p⁺–n’–junctions, which are fabricated as a

result of this implantation, are typically lower than those in ‘n⁺–p’–junctions due to the fact that in the n–‘base’ carrier lifetime is governed by the band-to-band CHCC recombination, which ensures an increased lifetime and the low dark current. As a result of the lower dark current, higher working temperature or a longer wavelength cut-off sensitivity threshold of photodiodes can be achieved.

Development of the photodiode technology based on ion implantation requires microstructural studies of the implanted material, and arsenic-implanted MCT is not an exception (Mollard et al. 2011; Lobre et al. 2014; Shi et al. 2016; Bonchuk et al. 2020). These studies allow for assessing the type and the density of implantation-induced structural defects, which play a key role in controlling the electrical properties of the as-implanted MCT (Lobre et al. 2014; Shi et al. 2016). Electrical studies, in their turn, allow for assessing the degree of activation of the implanted ions and for obtaining the information on the transport properties of the material. In MCT–based ‘p⁺–n’–junctions, however the high electrical conductivity of the n–region hinders obtaining this information due to a very large difference between electron and hole mobility. As a result, the effect of arsenic implantation on the electrical properties of MCT is often studied after implantation into p–type material (Izhnin et al. 2019). This approach presumes that the formation of implantation-induced structural defects proceeds similarly in the ‘base’ MCT layers with p and n–type conductivity. It is known, however, that defect structure of a semiconductor

✉ I. Izhnin
i.izhnin@carat.electron.ua

¹ Scientific Research Company “Electron-Carat”, Stryiska 202, Lviv 79031, Ukraine

² National Research Tomsk State University, Lenina 36, 634050 Tomsk, Russia

³ Ioffe Institute, Polytechnicheskaya 26, 194021 Saint-Petersburg, Russia

⁴ Institute of Metallurgy and Materials Science PAN, Reymonta 25, 30-059 Krakow, Poland

⁵ Hetman Petro Sahaidachny National Army Academy, Gvardijska 32, Lviv 79012, Ukraine

⁶ A. V. Rzhhanov Institute of Semiconductor Physics, SB RAS, Ac. Lavrentieva 13, 630090 Novosibirsk, Russia

⁷ Ya.S. Pidstryhach Institute for Applied Problems of Mechanics and Mathematics NASU, Naukova 3b, Lviv 79060, Ukraine

after the implantation is strongly affected by formation, migration and interaction of primary implantation defects, such as vacancies and interstitials. As p-type conductivity of the ‘base’ in ‘n⁺–p’-type structures in MCT is usually defined by intentionally introduced mercury vacancies, which are acceptors in this material, the aim of this work was to perform a direct comparison of nano-scale structure in arsenic-implanted n and p-type films to establish the possible effect of the initial defect structure on the results of the implantation.

Methods

For the studies, an MCT film was grown by molecular-beam epitaxy (MBE) at A.V. Rzhanov Institute of Semiconductor Physics (Novosibirsk, Russia) on a (013) CdTe/ZnTe/Si substrate. The growth cycle was controlled in situ by means of an ellipsometer (Yakushev et al. 2011). The ‘absorber’ layer of the film with the thickness 8.1 μm had constant composition $x = 0.22$, the graded-gap protective surface layer (400 nm) had composition at the surface $x = 0.46$. The film was doped with indium during the growth, and according to the results of the standard Hall-effect measurements performed at 77 K, the as-grown material had n-type conductivity with electron concentration $\sim 4 \cdot 10^{15} \text{ cm}^{-3}$. A piece cut from the film after the growth was subjected to thermal annealing (220 °C, 24 h) in helium atmosphere at low mercury pressure to generate mercury vacancies. As a result of the annealing, a p-type sample was fabricated with hole concentration $p = 5.1 \cdot 10^{15} \text{ cm}^{-3}$.

Both n-type (sample #1) and p-type (sample #2) samples were implanted with As⁺ ions with ion energy $E = 190 \text{ keV}$ and ion fluence $\Phi = 10^{14} \text{ cm}^{-2}$. The implantation was performed using IMC200 (Ion Beam Services, France) system. The structural studies were performed in bright-field transmission electron microscopy (BF-TEM) and high-resolution TEM (HRTEM) modes using Tecnai G2 F20, FEI Company microscope. Thin foils for the studies were cut out using

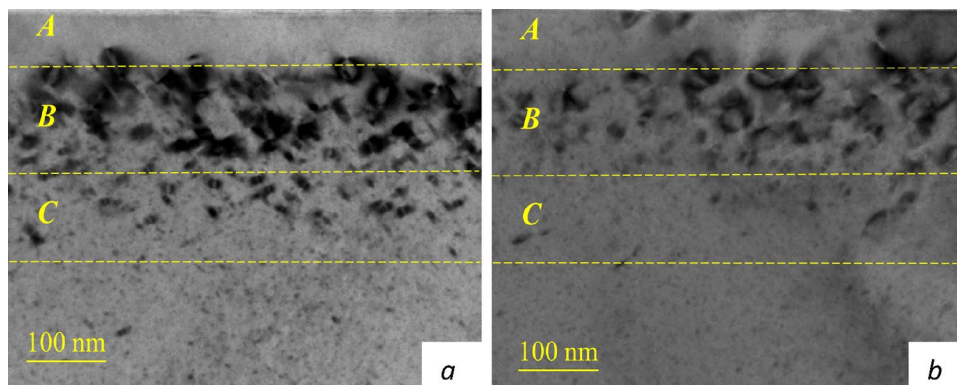
FEI Quanta 200 dual-beam focused ion (Ga⁺) beam machine equipped with Omniprobe™ lift-out system. The material under study was first covered with 300 nm-thick amorphous carbon layer that prevented the surface from the damage which could be inflicted by Ga⁺ ions used for the deposition of a Pt bar. Next, trench milling was done on both sides of the bar. The effect of Ga⁺ ions was minimized by limiting the beam current during the milling, starting from 20 nA, continuing with 7 nA, and finishing with 5 nA. The final polishing of the lifted lamella was done starting from 1 nA ion beam current, continuing with 0.3 nA, and finishing with 0.1 nA. The energy of Ga⁺ ions did not exceed 2 keV. The analysis of HRTEM images was carried out using direct and inverse Fast Fourier Transforms (FFT, IFFT).

Results

The defect pattern of the as-grown material similar to the one used in this study was investigated on numerous occasions (see, e.g., Bonchuk et al. 2020). Structural defects in this material were represented by single dislocations, small (< 6 nm in linear size) dislocation loops, stacking faults and lattice deformations. These defects did not contribute to the defect pattern in the implanted material, as their density was very low and sizes were small.

Figure 1 shows BF-TEM images of the cross-sections of both studied samples after the implantation. The implantation-damaged layer could be divided into three characteristic sub-layers. Top sub-layers A had thicknesses $\sim 70 \text{ nm}$ in both samples and possessed a low density of structural defects. Similar layers with a very low density of structural defects were first observed by Lobre et al. (2013). Their formation is explained by the partial re-structuring (recombination) of the implantation-induced defects that takes place during the process of implantation; this is a characteristic feature of materials with the strong ionic nature of the chemical bonds, which is the case for MCT (Lobre et al. 2013). Sub-layers A were followed by sub-layers B, which contained

Fig. 1 BF-TEM images of the cross-sectional views of samples #1 (n-type, **a**) and #2 (p-type, **b**). The samples were implanted with arsenic with $E = 190 \text{ keV}$ and $\Phi = 10^{14} \text{ cm}^{-2}$



‘large’ structural defects; the density of these defects was high. The thicknesses of sub-layers *B* equaled ~ 120 nm in both samples. Sub-layers *B* were followed by ~ 100 nm-thick sub-layers *C*, which contained ‘small’ extended defects; the density of these defects was low. These three sub-layers were followed by the layers containing quasi-point defects, which could not be visualized in BF-TEM mode and appeared as a uniform background. These quasi-point defects were first detected and identified by Lobre et al. (2013) on the basis of the results of Rutherford backscattering experiments performed on arsenic-implanted MCT.

Using the free SRIM software, www.srim.org we simulated profiles of implanted arsenic ions and displaced vacancies (conductivity type could not be considered in the simulations). Simulated value of projected ion range R_p equaled 93 nm. This value was much lower than the total depth of the implantation-damaged layers (330 nm for both samples according to Fig. 1), and the position of R_p corresponded to the upper parts of the sub-layers *B*. The simulated profile of generated vacancies, in its turn, had maximum at the depth ~ 30 nm, so the areas with the highest concentration of implantation-induced defects should have formed in both samples within the sub-layers *A*, which, according to Fig. 1, in reality were almost free of structural defects. Thus, according to the results of the simulations, the surface

layers with low defect density could have been expected to be much thinner than those observed experimentally. The actual defect pattern in the TEM images can be explained by the recombination of structural defects and partial restoration of the crystalline structure that proceeded during the process of implantation, as mentioned above.

Figure 2 shows HRTEM images of selected areas in sub-layers *A* of sample #1 (a) and sample #2 (b). Insets in Fig. 2a, b show FFT of the corresponding HRTEM images, while Fig. 2c, d shows corresponding IFFT images. Red arrows and dashed ovals in Fig. 2c, d mark dislocation loops; yellow arrows, single dislocations. As can be seen, for sample #1 (Fig. 2a, c) in sub-layer *A* one can observe isolated vacancy-type dislocation loop P_8 (3 nm in size) and interstitial-type loop P_{10} (2 nm), and some single dislocations against the background of almost perfect crystalline structure. For sample #2 (Fig. 2b, d) one can also observe isolated vacancy-type dislocation loops P_2 (3 nm) and P_3 (5 nm), again against the background of almost perfect crystalline structure. Solitary stacking faults and single dislocations are seen in both images, but the general defect density in this sub-layer was low in both samples.

Figure 3a shows an HRTEM image of a selected area in sub-layer *B* of sample #1 (n-type). Inset in Fig. 3a shows the corresponding FFT image, while Fig. 3b shows the

Fig. 2 HRTEM images of selected areas in sub-layers *A* of implanted n-type sample #1 (a) and p-type sample #2 (b) with insets showing their FFT images and images (c) and (d) showing corresponding IFFT images. Red arrows and dashed ovals in images (c) and (d) mark dislocation loops; yellow arrows, single dislocations

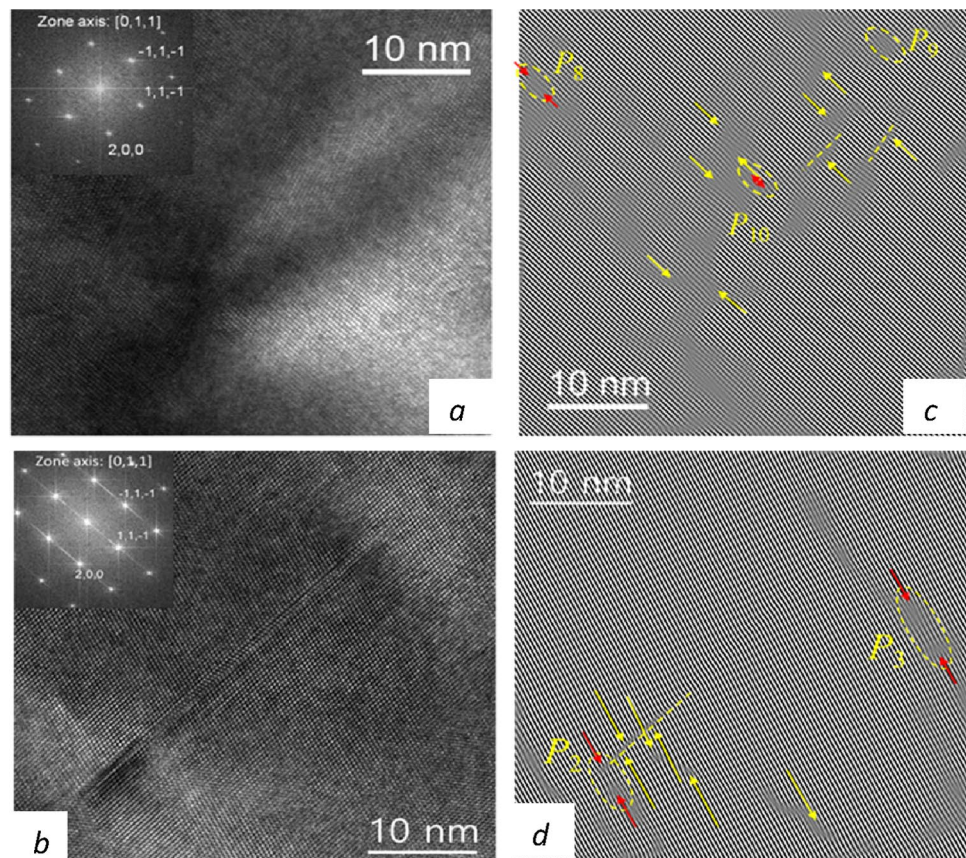
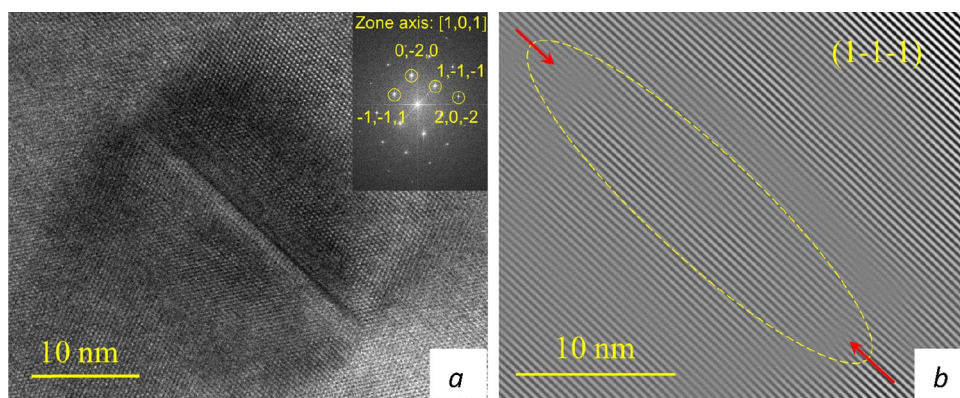


Fig. 3 HRTEM image of a selected area of sub-layer *B* in implanted *n*-type sample #1 (a) with inset showing its FFT image, and the corresponding IFFT image (b). Red arrows and a dashed oval in image (b) mark a dislocation loop



corresponding IFFT image. Red arrows and a dashed oval in Fig. 3b mark a large dislocation loop. According to both BF-TEM and HRTEM data, sub-layer *B* contained a high density of large extended structural defects, namely, dislocation loops with considerable sizes, single dislocations, and stacking faults. Large dislocation loops were the dominating defects in this layer. For example, a vacancy-type dislocation loop shown in Fig. 3b had a linear size 28 nm.

Figure 4a shows HRTEM image of a selected area of sub-layer *B* in sample #2. Inset in Fig. 4a shows the corresponding FFT image, while Fig. 4b, c shows the corresponding IFFT images. Red arrows and dashed ovals in Fig. 4b, c mark dislocation loops; yellow arrows, single dislocations. As follows from Fig. 4, sub-layer *B* in sample #2 contained high density of large extended structural defects, defect complexes and agglomerates. The most typical defects were large dislocation loops, other defects were single dislocations, stacking faults and lattice deformations. Dark grey areas in Fig. 4a show spots with considerable lattice disorder. IFFT images in Fig. 4b, c show vacancy- (P_4 , P_5) and interstitial-type (P_6) dislocation loops. These loops were large in size: for P_4 , the size of the loop was ~ 10 nm; for P_5 , 12 nm; for P_6 , ~ 15 nm. The

loops were accompanied by numerous dislocations and lattice deformations.

Figure 5 shows HRTEM images of selected areas in sub-layers *C* of sample #1 a and sample #2 b. Insets in Fig. 5a, b show FFT of the corresponding images, while Fig. 5c, d shows corresponding IFFT images. Red arrows and dashed ovals in Fig. 5c, d mark dislocation loops; yellow arrows, single dislocations. The defects in sub-layer *C* appeared to be smaller in size than those in sub-layer *B*. Only one dislocation loop is seen in each IFFT image in Fig. 5, for sample #2, it is marked as P_7 . The linear size of these loops was ~ 10 nm. Some single dislocations were visible in IFFT images, but the general defect density in sub-layer *C* appeared to be low.

According to the data presented in Figs. 1, 2, 3, 4, 5, the effect of arsenic implantation on the structural quality of MCT appeared to be very similar in *n* and *p*-type material. BF-TEM studies showed that the defect layers produced by the implantation were similar in *n* and *p*-type samples in terms of the thicknesses of the formed defect layers and of the number of defect sub-layers. Top sub-layers *A* had thicknesses ~ 70 nm in both samples and possessed a low density of structural defects. Sub-layers *B* (~ 120 nm in

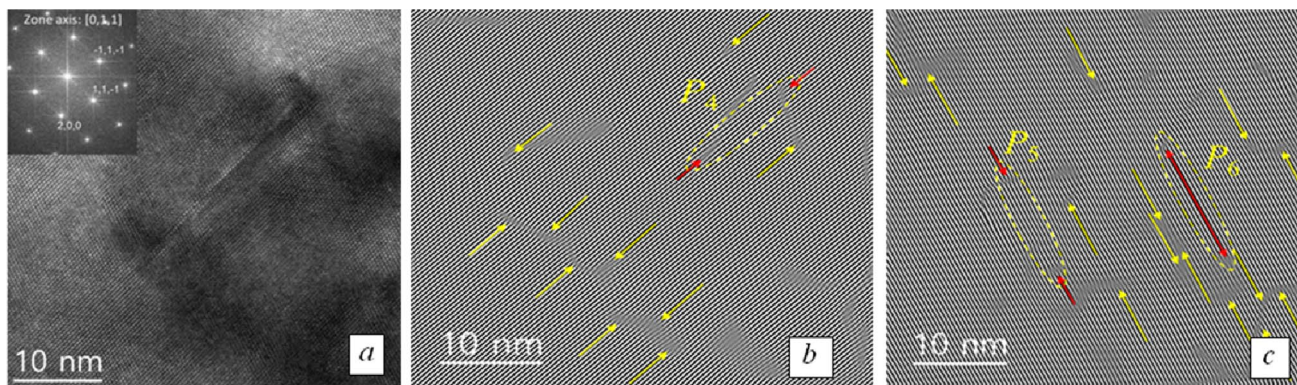
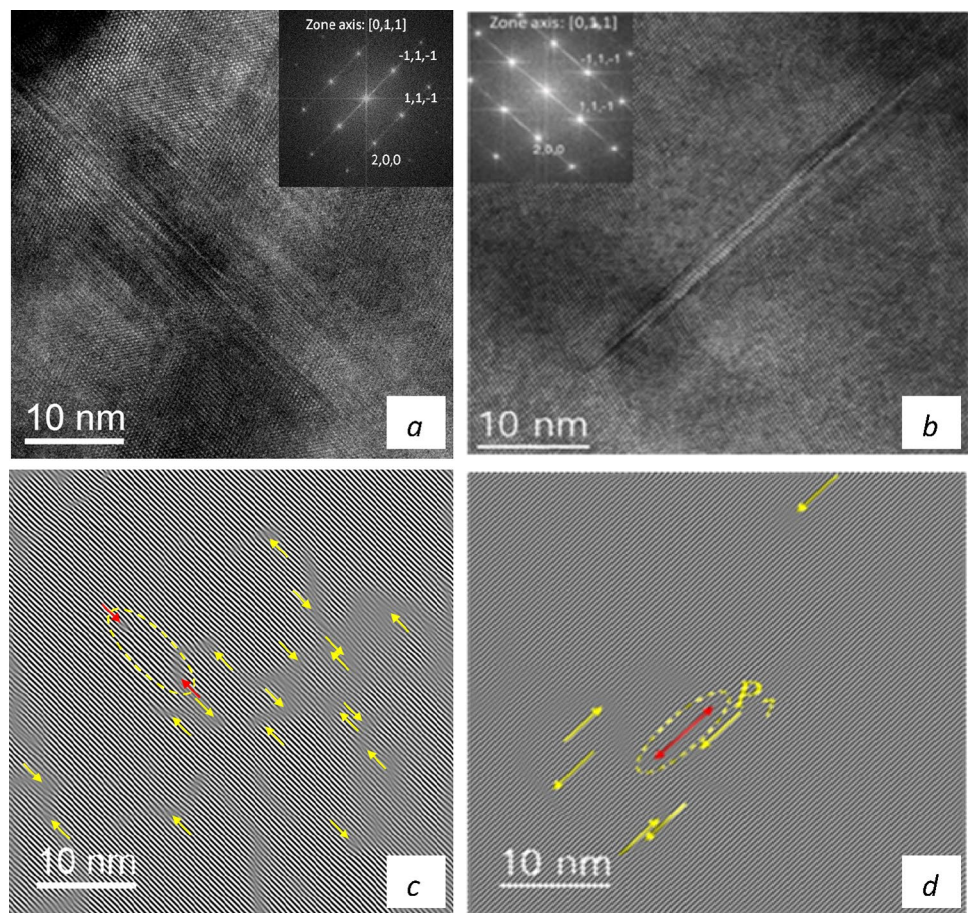


Fig. 4 HRTEM image of a selected area of sub-layer *B* in implanted *p*-type sample #2 (a) with inset showing its FFT image, and corresponding IFFT images (b, c). Red arrows and dashed ovals mark dislocation loops; yellow arrows, single dislocations

Fig. 5 HRTEM image of selected areas in sub-layers *C* in implanted n-type sample #1 (a) and p-type sample #2 (b) with insets showing their FFT patterns and images (c) and (d) showing corresponding IFFT patterns. Red arrows and dashed ovals in images (c) and (d) mark dislocation loops; yellow arrows, single dislocations



both samples) contained ‘large’ structural defects with high densities. Sub-layers *C* were ~ 100 nm-thick and contained ‘small’ extended defects with lower densities. HRTEM studies showed that the defect layers produced by the implantation were also similar in n and p-type samples in terms of the types and size of the induced defects. Sub-layers *A* contained isolated dislocation loops of small size, stacking faults and some single dislocations against the background of almost perfect crystalline structure. Sub-layers *B* contained high density of large extended structural defects along with defect complexes and agglomerates. The defects in sub-layers *C* were smaller both in size and density than those in sub-layers *B*.

As the final goal of the performed implantation was the formation of ‘p⁺–n’-junctions suitable for the fabrication of photodiodes, we also studied the electrical properties of the implanted material. For that purpose, we measured the magnetic field *B* dependences of the Hall coefficient and the conductivity in the $B = 0.01$ – 1.5 T range at 77 K. The obtained data were analyzed with the use of the discrete mobility spectrum analysis (DMSA, Izhnin et al. 2019); this technique allows for determining the number of carrier species and their parameters: concentration, mobility and partial conductivity. In particular, the analysis of sample #1

(n-type) showed that its conductivity before the implantation was dominated by high-mobility electrons (majority carriers) with average (reduced to the total thickness of the film) concentration $3.9 \cdot 10^{15} \text{ cm}^{-3}$; mobility, $87,500 \text{ cm}^2/(\text{V s})$; and average partial conductivity $54.6 (\text{Ohm cm})^{-1}$ with directly measured total conductivity equaling $56.6 (\text{Ohm cm})^{-1}$. Electrons with intermediate mobility were also detected; these are typically located in the transitional layer at the film/buffer layer interface (Varavin et al. 2001). In sample #2 (p-type) before the implantation the conductivity was dominated by heavy holes with average concentration $5.07 \cdot 10^{15} \text{ cm}^{-3}$, mobility $384 \text{ cm}^2/(\text{V s})$, and average partial conductivity $0.31 (\text{Ohm cm})^{-1}$ with directly measured total conductivity equaling $0.325 (\text{Ohm cm})^{-1}$. Other carriers detected in this sample included light holes, transitional-layer intermediate-mobility electrons and the high-mobility electrons, which in this case acted as minority carriers.

The results of the DMSA of the $R_H(B)$ and $\sigma(B)$ dependences for the implanted samples are shown in Fig. 6. In sample #1 with original n-type, the implantation resulted in the formation of the n⁺–n-structure, where the n-region represented a part of the ‘base’ that was not affected by the implantation, while the formation of the n⁺-region was its direct result. The dominating contribution to the

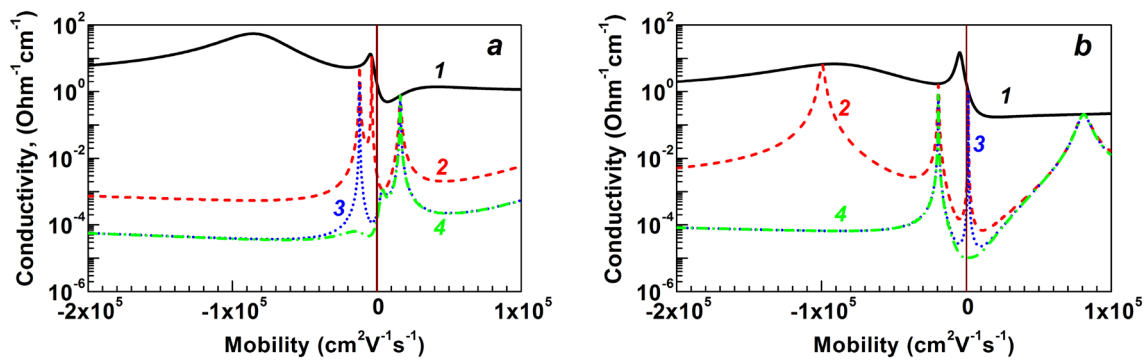


Fig. 6 Mobility spectrum envelopes (MSEs) obtained with the use of DMSA for n-type sample #1 (a) and p-type sample #2 (b) after ion implantation. Curves in graphs (a) and (b) show envelopes: 1, pri-

mary envelopes; 2, 3 and 4, envelopes after the first, the second and the third discretization steps, respectively

conductivity in this sample was that by the high-mobility electrons of the n-region, just because of their high mobility values and the large thickness of this region. The average partial conductivity provided by these electrons equaled $55.0 \text{ (Ohm cm)}^{-1}$ with the total conductivity of the structure equaling $74.5 \text{ (Ohm cm)}^{-1}$. These electrons showed off in the primary MSE (Fig. 6a, curve 1) in the mobility peak at $85,700 \text{ cm}^2/(\text{V s})$. These carriers obviously originated in the residual/introduced donors of the n-base, in our case, indium atoms. Sample #1 also contained the intermediate-mobility ($12,000 \text{ cm}^2/(\text{V s})$) electrons with the average concentration $3.1 \cdot 10^{15} \text{ cm}^{-3}$ and the average partial conductivity $5.98 \text{ (Ohm cm)}^{-1}$, but of our primary interest was the contribution to conductivity by the low-mobility electrons. These carriers are known to originate in the atoms of interstitial mercury captured by implantation-induced structural defects, such as dislocation loops visualized in our nano-scale structural studies (Figs. 1, 2, 3, 4, 5 see also Izhnin et al. 2018, 2019). In sample #1, these electrons provided partial conductivity $11.7 \text{ (Ohm cm)}^{-1}$, as the primary MSEs (Fig. 6a) showed a sharp peak at mobility value $3590 \text{ cm}^2/(\text{V s})$, which allowed for determining their average concentration as $2.03 \cdot 10^{16} \text{ cm}^{-3}$.

In sample #2 with initial p-type conductivity (Fig. 6b), ion implantation resulted in the formation of an n^+-n-p structure. In this structure, the p-type region represented the ‘base’ that was not affected by the implantation, while the n^+-n -region formed as its result. The dominating contribution to the conductivity was that by the low-mobility [$4650 \text{ cm}^2/(\text{V s})$] electrons, which can be seen in Fig. 6b (curve 1), where the corresponding mobility peak is clearly dominating. They provided average partial conductivity $14.9 \text{ (Ohm cm)}^{-1}$ with the total measured conductivity equaling $24.46 \text{ (Ohm cm)}^{-1}$. The average concentration of these electrons equaled $2.00 \cdot 10^{16} \text{ cm}^{-3}$. The similarity in the concentration of the low-mobility electrons in implanted samples #1 and #2 agreed with the data provided by the structural

studies and confirmed that the process of the formation of these implantation-induced defects was not affected by the conductivity type of MCT. Other carriers detected in this sample included the high-mobility ($99,600 \text{ cm}^2/(\text{V s})$) and intermediate-mobility ($19,400 \text{ cm}^2/(\text{V s})$) electrons; their average concentration equaled $4.15 \cdot 10^{14} \text{ cm}^{-3}$ and $5.50 \cdot 10^{14} \text{ cm}^{-3}$, respectively. The high-mobility electrons in the n-layers of the n^+-n-p structures are known to originate in the residual (or intentionally introduced, as in our case with indium doping) donors that determine the conductivity after the atoms of Hg_1 had diffused into the crystal and annihilated with mercury vacancies that defined the p-type conductivity before the implantation (Izhnin et al. 2018). The intermediate-mobility electrons (or at least a part of them) originated in the donor complexes that Hg_1 atoms form with quasi-point defects induced by the implantation (Izhnin et al. 2019).

It can be noted that though it could appear from both the BF-TEM and HRTEM data that in sample #2 the density of defects in all sub-layers was lower than that in sample #1 and the size of dislocation loops was smaller, this observation was not supported by the results of the electrical studies. Considering the locality of TEM, before any serious conclusions can be drawn in this respect, a larger number of samples should be investigated. This is a subject for future studies.

Conclusion

In conclusion, the effect of arsenic implantation on the formation of defects appeared to be very similar in n and p-type $\text{Hg}_{0.78}\text{Cd}_{0.22}\text{Te}$. BF-TEM studies showed that the defect layers produced by the implantation were similar in n and p-type samples in terms of the thicknesses of the implantation-damaged layers. These layers could be divided into three characteristic sub-layers. The top sub-layers A had

thicknesses ~ 70 nm in both samples and possessed a low density of structural defects. Sub-layers *A* were followed by sub-layers *B*, which contained large structural defects with high densities. The thicknesses of the sub-layers *B* equaled ~ 120 nm in both samples. The sub-layers *B* were followed by ~ 100 nm-thick sub-layers *C*, which contained small structural defects with lower densities. HRTEM studies showed that the defect layers produced by the implantation were also similar in n and p-type samples in terms of the types and size of the defects. Sub-layers *A* contained isolated dislocation loops of small size, stacking faults and solitary single dislocations against the background of almost perfect crystalline structure. Sub-layers *B* contained high density of large dislocation loops along with defect complexes and agglomerates. Defects in sub-layers *C* were smaller in size and density than those in the sub-layer *B*. Similarity in defect pattern in n and p-type samples after the implantation was confirmed by the results of the electrical studies, which showed almost identical concentrations of electrons in implantation-induced n^+ -layers.

Compliance with ethical standards

Conflict of interest On behalf of all authors, the corresponding author states that there is no conflict of interest.

References

- Bazovkin VM, Dvoretzky SA, Guzev AA et al (2016) High operating temperature SWIR p(+)-n FPA based on MBE-grown HgCdTe/Si(013). *Infr Phys Technol* 76:72–74
- Bommena R, Ketharanathan S, Wijewarnasuriya PS et al (2015) High-performance MWIR hgcdte on Si substrate focal plane array development. *J Electron Mater* 44:3151–3156
- Bonchik OY, Savvitskiy HV, Izhnin II et al (2020) Nano-size defect layers in arsenic-implanted and annealed HgCdTe epitaxial films studied with transmission electron microscopy. *Appl Nanosci* 10:4971–4976
- Gravrand O, Mollard L, Largeron C et al (2009) Study of LWIR and VLWIR focal plane array developments: comparison between p-on-n and different n-on-p technologies on LPE HgCdTe. *J Electron Mater* 38:1733–1740
- Guinedor P, Brunner A, Rubaldo L et al (2019) Low-frequency noises and DLTS studies in HgCdTe MWIR photodiodes. *J Electron Mater* 48:6113–6117
- Izhnin II, Fitsych EI, Voitsekhovskii AV et al (2018) Defects in arsenic-implanted p^+ -n and n^+ -p-structures based on MBE-grown CdH-gTe films. *Russ Phys J* 60:1752–1757
- Izhnin II, Mynbaev KD, Voitsekhovskiy AV et al (2019) Arsenic-ion implantation-induced defects in HgCdTe films studied with hall-effect measurements and mobility spectrum analysis. *Infr Phys Technol* 98:230–235
- Lobre C, Jalabert D, Vickridge I et al (2013) Quantitative damage depth profiles in arsenic implanted HgCdTe. *Nucl Instrum Meth B* 313:76–80
- Lobre C, Jouneau PH, Mollard L et al (2014) Characterization of the microstructure of HgCdTe with p-type doping. *J Electron Mater* 43:2908–2914
- Mollard L, Destefanis G, Bourgeois G et al (2011) Status of p-on-n arsenic-implanted HgCdTe technologies. *J Electron Mater* 40:1830–1839
- Park JH, Pepping J, Mukhortova A et al (2016) Development of high-performance eSWIR HgCdTe-based focal-plane arrays on silicon substrates. *J Electron Mater* 45:4620–4625
- Shi CZ, Lin C, Wei Y et al (2016) Barrier layer induced channeling effect of As ion implantation in HgCdTe and its influences on electrical properties of p-n junctions. *Appl Opt* 55:D101–D105
- Varavin VS, Kravchenko AF, Sidorov YuG (2001) A study of galvanomagnetic phenomena in MBE-grown n-Cd_xHg_{1-x} Te films. *Semiconductors* 35:992–996
- Yakushev MV, Brunev DV, Varavin VS et al (2011) HgCdTe heterostructures on Si (310) substrates for MWIR infrared photodetectors. *Semiconductors* 45:385–391

Publisher's Note Springer Nature remains neutral with regard to jurisdictional claims in published maps and institutional affiliations.